Bi-Phase Compound-Gaussian Mixture Model of Sea Clutter and Scene-Segmentation-Based Target Detection

Xiang Liang [ID], Peng-Lang Shui [ID], *Senior Member, IEEE*, and Hong-Tao Su [ID]

Abstract—In high-resolution maritime surveillance radars, sea clutter exhibits highly spatial heterogeneity due to modulation of long waves with wavelengths longer than the width of one range cell. Compound-Gaussian model (CGM) fails to characterize the heterogeneous high-resolution sea clutter in both amplitude distribution and Doppler spectrum. In this article, a bi-phase compound-Gaussian mixture model (BP-CGMM) is proposed to characterize the heterogeneous sea clutter. In the BP-CGMM, spatial resolution cells are grouped into two disjoint sets, and the sea clutter in each set is represented by one CGM with inverse Gamma-distributed texture. The spectral heterogeneity indicates that sea clutter vectors at spatially adjacent resolution cells in one set share the same speckle covariance matrix, while that at two adjacent spatial cells separated in the two sets often have different speckle covariance matrices. The BP-CGMM is validated by a mass of measured high-resolution sea clutter data. Moreover, under the BP-CGMM, a detection method based on batch test is given to detect sea-surface small targets, which is composed of scene segmentation, by the aid of Bayesian threshold and morphological filtering, and adaptive generalized likelihood ratio test linear-threshold detector (GLRT-LTD) separately in each set. The detection method is verified by measured data with small targets under test. The experimental results show that it attains better detection performance than the adaptive GLRT-LTD under the CGM of sea clutter.

Index Terms—Compound-Gaussian mixture model, heterogeneous high-resolution sea clutter, modulation of long waves, scene segmentation, spectral heterogeneity.

NOMENCLATURE

K	Length of sliding window.
$c(n)$	Sea clutter time series.
Δt	Pulse repetition interval.
T	Texture coherent length.
$\hat{\tau}(n)$	Estimated texture time series.
f_d	Normalized Doppler offset.
σ_d	Normalized Doppler bandwidth.
$\mathbf{r}$	Coordinate of a resolution cell.
$\mathbf{z_r}$	Sea clutter vector.
Ω	Universal set of $\mathbf{r}$.
Ω_0	Set of resolution cells in dim region.
Ω_1	Set of resolution cells in bright region.
$\mathbf{M}$	Speckle covariance matrix.
z	Amplitude of sea clutter.
pdf	Probability density function.
CDF	Cumulative distribution function.
f	pdf of the amplitude.
F	CDF of the amplitude.
η	Scale parameter.
λ	Shape parameter.
α	Mixture ratio.
ECDF	Empirical CDF of amplitude.
Epdf	Empirical pdf of amplitude.
d_B	Bhattacharyya distance.
$d_{Log-K-S}$	Log-Kolmogorov–Smirnov distance.
N	Number of samples.
M	Number of pulses in a received vector.
$p(\tau)$	Pdf of texture.
ξ_i	Test statistic in the set Ω_i.
GLRT-LTD	Generalized likelihood ratio test linear-threshold detector.
$\xi_{\mathrm{GLRT-LTD}}$	Test statistic of adaptive GLRT-LTD.

I. INTRODUCTION

AIRBORNE/SPACEBORNE synthetic aperture radar (SAR) systems [1], [2] and traditional maritime surface surveillance radars operating at scan or dwelling mode [3], [4], are two types of complementary sensors in ocean and ship surveillance systems. SAR systems can provide high-spatial resolution images of a wide surveillance area, containing subtle shape information of targets such as ships [1], [2], [5]–[10]. But it is difficult to collect information in real time for SAR systems [8]. Surface surveillance radars can collect information in real time in a relatively small surveillance area with high range resolution but low azimuth resolution which makes it difficult to provide subtle shape information of targets [3], [4]. Both types of sensors detect targets against backscattering from sea surface, namely, speckles in SAR images and sea clutter in surface surveillance radars [1]–[5]. In SAR systems, coherent integration of second-order or subsecond-order is performed in imaging, and thus, the intensity models of reflectance coefficients are sufficient for target detection in SAR

images [5]. In surface surveillance radars, subtle amplitude models and Doppler spectral characteristics are necessary for moving small target detection [3]. Due to systematic discrepancies, target detection in SAR systems depends on image processing techniques [5]–[10], whereas target detection in surface surveillance radars is based on adaptive detection and integration of target returns within several tens of milliseconds [11]–[13]. This article focuses on sea clutter modeling and moving small target detection in maritime surface surveillance radars. For small target detection [3], [4], [14], a valid and feasible technique to enhance signal-to-clutter ratio (SCR) is to match the range resolution of radar to the size of interested small targets [3]. As a result, high range resolution leads to heterogeneity and non-Gaussianity of sea clutter, which degrades the detection performance of existing adaptive coherent detection methods due to model mismatch, especially in moderate and high sea states [15]. Therefore, the detection performance improvement of small targets depends on subtle high-resolution sea clutter model and utilization of the model in design of detection methods.

Sea clutter modeling plays an irreplaceable role in design and signal processing of maritime radars [16]. Sea clutter results from the interaction between incident electromagnetic (EM) waves and time-evolving sea surface [17]. Characteristics of sea clutter are gradually revealed in two ways: statistical recognition by radar data analysis [18]–[20] and physical recognition by the EM scattering mechanisms analysis [21]–[24]. All efforts yield various mathematical models of sea clutter for maritime radars. Early sea clutter models focus on the statistical fitting of amplitude distributions, for instance, the Rayleigh distributions, the log-normal distributions, and Weibull distributions, which are the foundation of noncoherent radar detection in sea clutter [19]. Early physical recognition of sea clutter focuses on the intensity prediction of sea clutter from radar parameters, viewing geometry, and sea states, which supports the design of radar systems [16].

Compound-Gaussian model (CGM) originates from the physical fact that surface waves with wavelengths comparable with radar wavelength result in Bragg scattering whose intensity is modulated by the underlying large-scale waves [17]. In the CGM, complex sea clutter time series from a spatial resolution cell is modeled as a product of a fast-varying complex Gaussian speckle random series and a slow-varying positive texture random series, and the two series are mutually independent [16]. In a coherent processing interval (CPI) of tens of milliseconds, the texture process is reduced to a random constant, and the CGM degenerates to the spherical invariant random vector (SIRV) model [14]. Different types of texture distributions are successively introduced, such as Gamma distributions, inverse Gamma distributions, log-normal distributions, and inverse Gaussian distributions [11]. Owing to the mathematical tractability of the conditional Gaussian expression of the SIRV model, the optimum or near-optimum coherent detectors are sequentially presented [11]–[13].

The CGM is based on the three basic assumptions: Gaussianity of speckle, homogeneity of texture, and their mutual independence. The first assumption originates from the application of the central limit theorem, considering that the Bragg scattering in a spatial resolution cell is the summation of backscattering echoes from masses of scatterers on the sea surface [17], which always holds for both low-resolution and high-resolution radars. The other two assumptions are invalid in some cases. As radar range resolution gets higher, the variation of texture and speckle spectral shape exhibits correlated and periodic behaviors relevant to long waves, implying invalid homogeneity assumption of texture and independence assumption between speckle and texture [17]. Therefore, the CGM fails to characterize long-wave modulated high-resolution sea clutter to some extent. In [14], [25], correlated texture and texture-dependent Doppler spectral characteristics are considered to simulate high-resolution sea clutter.

Several mixture models have been developed to account for heavy-tailed distributions and variation of Doppler spectra in high-resolution sea clutter [18]–[20]. The KA model is a mixture of the CGM with Gamma-distributed texture and a discrete Poisson process of sea spikes [18]. The KK and WW models are the mixtures of two K-distributions and two Weibull distributions [19], wherein one of the two distributions is for sea spikes. Recently, several bimodal coherent sea clutter models are proposed to characterize varying Doppler spectra with time and range [20]. These mixture models exhibit satisfactory goodness-of-fit on measured data by integrating the contribution of regular Bragg resonance and fast scatterers related to sea spikes in backscattering echoes from sea surface. Nevertheless, it is challenging to develop effective coherent detectors from these models due to the absence of mathematical tractability. In view of the lifetime of sea spikes from several tenths of a second to several seconds, false alarms from sea spikes are mainly excluded by interscan processing [14]. This article focuses on modeling long-wave modulated sea clutter excluding sea spikes, and relevant detection method.

The statistical consistency of clutter at the cell under test (CUT) and reference cells (RCs) is a prerequisite of adaptive detection [15]. Mostly, RCs are composed of spatial resolution cells around CUT under homogeneous assumption. Whereas, a general case is that covariance matrices of the CUT and the RCs coincide only up to a scale factor, which is referred to as a partially homogeneous environment [26]. The variant scale factors, namely, texture components, are modeled as a random variable under the SIRV model [11]–[13]. The more complicated case is that some of the RCs are contaminated, which results in a heterogeneous environment with spatially variant amplitude distributions and spectral shapes [27]–[30]. The heterogeneity probably comes from many sources, such as interfering targets, discrete outliers, and clutter edges [27]. For different cases, various methods have been developed to estimate the clutter characteristics at the CUT, including the cell-clustering method for selection of RCs [27], the knowledge-aided methods [28], the Bayesian methods using the prior structural information to compensate inefficient RCs [29], and outliers-censoring method [30], which all attain better performance owing to their subtle clutter models. Nevertheless, these methods all suffer from high-computation complexity due to their statistic-based strategies to deal with heterogeneous environments.

As a major contribution, a bi-phase compound-Gaussian mixture model (BP-CGMM) is proposed to characterize the bi-phase property of sea clutter in both amplitude distribution and Doppler spectrum. The bi-phase property of sea clutter is statistically analyzed based on measured datasets and physical interpretation. Due to the modulation of temporal-spatially evolving long waves, the amplitude of sea clutter exhibits alternant bright or dim stripes on the range-time plane at the dwelling mode and bright or dim patches on the range-azimuth plane at the scan mode. The spectral shapes of the parts with higher intensity and the parts with lower intensity exhibit distinct Doppler offsets and bandwidths. In BP-CGMM, all resolution cells in a patch of sea surface are grouped into two sets wherein one consists of bright stripes or patches, and the other consists of dim stripes or patches. Sea clutter in each set is modeled by a CGM with inverse Gamma-distributed texture, and in each set the sea clutter vectors at adjacent cells share the same spectral shape. The two CGMs in the BP-CGMM are restricted in two disjoint sets of resolution cells, which provide mathematical tractability in designing the optimum coherent detectors. In a mass of measured X-band sea clutter datasets [31], the fitting performance of the BP-CGMM is superior to the CGM, particularly in moderate and high sea states. In most of the datasets, the two estimated shape parameters of the BP-CGMM are larger than the estimated shape parameter of the CGM. The result implies that the bi-phase mixture model cuts down texture fluctuation in long-wave modulated sea clutter, which is beneficial to target detection in sea clutter.

As a minor contribution, a scene-segmentation-based target detection scheme via batch test is given under the BP-CGMM to improve the detection performance of low-velocity small targets in surface surveillance radars. In the scheme, received data from a section within thirty degrees in the scan mode or in a time interval within several seconds in the dwelling mode are first stored for batch test. A delay of several seconds is tolerable in tracking of sea-surface targets due to their low velocities [32]. The parameters of the BP-CGMM are estimated from truncated data in the batch. Then the resolution cells are grouped into two sets based on Bayesian threshold followed by mathematical morphological filtering [8]. Finally, the adaptive generalized likelihood ratio test linear-threshold detector (GLRT-LTD) [12] is separately applied in each set for target detection. The proposed scheme is verified by measured datasets with test targets. The results show that it attains better detection performance than the adaptive GLRT-LTD under the CGM. The improvement of detection performance results from two advantages of the BP-CGMM, lower detection thresholds in individual sets and intraclass selection of RCs.

The remaining parts of this article are organized as follows. In Section II, the BP-CGMM of high-resolution sea clutter is proposed and verified by a mass of measured radar data. Section III presents a scene-segmentation-based target detection scheme under the BP-CGMM. Section IV reports the experimental results of the proposed target detection scheme on measured data. Finally, Section V concludes the article.
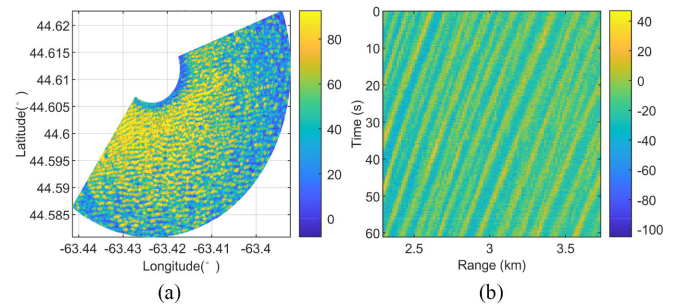

Fig. 1. Intensity maps of measured high-resolution sea clutter data in decibels. (a) Dataset "19931106-183151-surv" from the IPIX database at the scan mode [33]. (b) Dataset "CFC14-016" from the CSIR database at the dwelling mode [31].

II. Bi-Phase Compound-Gaussian Mixture Model of High-resolution Sea Clutter

As the spatial resolution of maritime radars gets higher, sea clutter data exhibits strong heterogeneity in space, time, and spectrum. In this section, the bi-phase behaviors of sea clutter in both texture and Doppler spectrum are presented and analyzed by measured datasets. Based on these behaviors, a BP-CGMM is proposed to characterize long-wave modulated high-resolution sea clutter. The fitting performance on the amplitude of a mass of measured datasets shows that the BP-CGMM can model high-resolution sea clutter better than the CGM, especially in moderate and high sea states.

A. Bi-Phase Behaviors of Heterogeneous Texture and Physical Interpretation

Fig. 1(a) illustrates the intensity of sea clutter on the range-azimuth plane from the IPIX database [33] collected at scan mode, and Fig. 1(b) illustrates the intensity of sea clutter on the range-time plane from the CSIR database [31] collected at the dwelling mode. The radar and environmental parameters of the two datasets are listed in Table I. The two datasets were collected in high sea states by X-band radars with different polarizations. Fig. 1 illustrates the intensity maps of sea clutter, where discernible patterns due to long-wave modulation can be observed from different perspectives. Fig. 1(a) exhibits a scaly pattern of intensity variation resulting from an instantaneous sea surface, which is relevant to significant height variation in space due to the superposition of long waves with different wavelengths and travel directions [14]. In Fig. 1(b), the radar is stared with an angle deviation of $17.2°$ to the wave direction, and the movements of long waves result in a striped pattern of the intensity on the range-time plane. As shown in Fig. 1, the regular patterns invalidate the homogeneity assumption of texture. Therefore, it is crucial to model spatial-temporal textures of high-resolution sea clutter.

To examine the characteristics of long-wave modulated texture at dwelling mode, texture time series are estimated from time series of sea clutter at each range cell by a sliding averaging
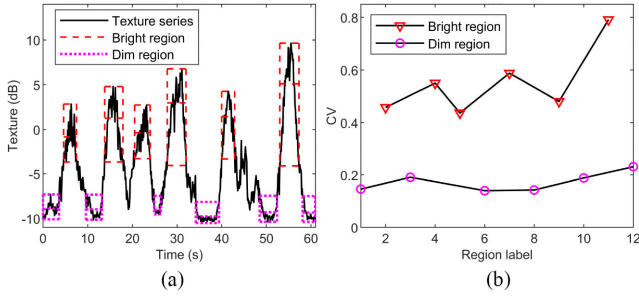
Fig. 2.   Bi-phase property illustration of the texture heterogeneity in long-wave modulated sea clutter. (a) Estimated texture time series at a range cell and extracted bright regions and dim regions. (b) CV of the texture in the bright regions and dim regions.

TABLE I
RADAR AND ENVIRONMENTAL PARAMETERS OF THE TWO DATASETS

Parameter	19931106-183151-surv	CFC14-016
Database	IPIX	CSIR
Operation mode	Scan	Dwelling
Polarization	HH	VV
Pulse repetition frequency (PRF)	800 Hz	5000 Hz
Tx. bandwidth	5 MHz	10 MHz
Tx. frequency	9.39 GHz	9 GHz
Antenna height	30.48 m	56 m
Antenna elevation	-0.85°	-1.26°
Range	711 m-3471 m	2301 m-3741 m
Radar location	63.43°W, 44.62°N	20.29°E, 34.62°S
Wave period	10 s	13 s
Significant wave height	3.36 m	3.11 m
Sea state (Beaufort scale)	4	4

method [17], where the length of the sliding window is determined by texture coherent length (TCL) and the pulse repetition interval (PRI). Let $c(n)$ be sea clutter time series received at a range cell with a PRI Δt. Then, the texture time series at a range cell is estimated by

$$\hat{\tau}(n) = \frac{1}{K} \sum_{k=-K/2}^{K/2-1} |c(n+k)|^2, K = \left[\frac{T}{\Delta t} \right] \qquad (1)$$

where K is the length of sliding window, and T is the TCL considered to be several hundreds of milliseconds for X-band high-resolution sea clutter [34], which ensures the precision of the estimated texture series. Fig. 2(a) illustrates the estimated texture time series at the 89th range cell of the dataset in Fig. 1(b), where the PRI is 0.2 ms, and K is taken as 500. The texture varies from -10.8 to 9.7 dB, and the noise of the radar receiver is negligible with the level of -22.5 dB [35]. The texture series exhibits quasi-periodic fluctuations with a period of 12 s which basically accords with the average wave period of 13 s in Table I. In Fig. 1(b), the texture patterns are composed of alternative bright stripes of high intensity and dim stripes of low intensity. For the

texture time series at each range cell and in each period, 40% largest samples form the bright region, 40% smallest samples form the dim regions, and 20% intermediate samples form the transition regions. As shown in Fig. 2, the texture time series with about six periods yields six bright regions marked by the dashed red rectangles, six dim regions marked by the dotted magenta rectangles, and the transition regions are neglected to avoid the extra error introduced by the subjective classification. In each period of long waves, the texture fluctuates around two centers. One center is the average value of the texture in the bright region indicated by the horizontal dashed line segment in the middle of the red rectangle. The other is the average value of the texture in the dim region indicated by the horizontal dotted line segment in the middle of the magenta rectangle. Therefore, the probability density function (pdf) of the texture tends to be bimodal instead of unimodal, which is referred to as the bi-phase property of the texture heterogeneity in long-wave modulated sea clutter.

The bi-phase property of texture can be interpreted by several kinds of modulation of long waves. The tilt modulation changes the local incident angle along the long wave profile, the hydro-dynamic modulation roughens the sea surface around wave crest to change the reflectance coefficients of the sea surface, and the range modulation changes the area of sea surface projecting to a range cell along the radar line of sight [21]. Regular patterns of texture are observed in many measured datasets, and some attempts were made to characterize them [36], [37].

The texture of each bright or dim region can be roughly characterized by the average value and the coefficient of variation (CV), which is the ratio of the standard deviation to the average value. The CV reflects the texture fluctuation extent in a region, and a larger CV means more violent fluctuation. The height of the rectangle reveals the dynamic range of the texture in each region in Fig. 2(a), and the CVs in the bright regions and dim regions are plotted in Fig. 2(b). All the dim regions have smaller average values and CVs, while all the bright regions have larger average values and CVs. The larger CVs of bright regions can be interpreted from the spike events occurring near the turbulent region at wave crests [38]. The bright region often corresponds to the radar returns from the wave crest in space. Due to the impact of wave–wave and wave–wind interactions, the intense but unstable spike events, such as quasi-specular facets, whitecaps, and bound waves, have short lifetimes from 0.5 to 2 s [35]. The frequent birth and death of spike events at wave crest induce a drastic fluctuation of the texture in the bright region. The dim regions exhibit contrastively small CVs resulting from the infrequent occurrences of spike events in wave troughs which often correspond to dim regions. Regarding the bi-phase property of heterogeneous textures, bimodal pdfs are a better choice to characterize texture statistics than commonly used unimodal pdfs.

B. Bi-Phase Behaviors of Doppler Spectral Heterogeneity

In the CGM, the amplitude distribution of sea clutter is determined by the texture statistics, and the Doppler spectral shape of sea clutter is mainly determined by the speckle temporal correlation. Different from the texture, whose characteristics are
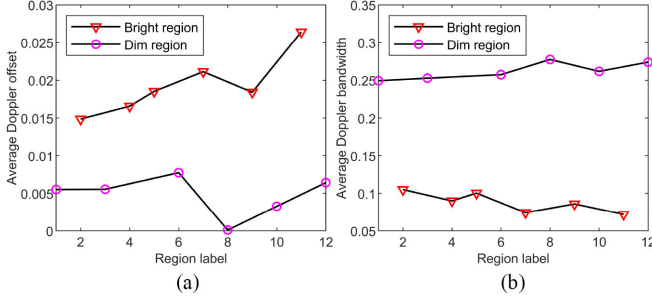
Fig. 3. Bi-phase property illustration of the Doppler spectral shapes of sea clutter. (a) Average Doppler offsets. (b) Average Doppler bandwidths.

relevant to swells and large-scale wind waves, speckle characteristics are relevant to capillary waves and small-scale wind waves [16]. The spectral shape of sea clutter can be roughly measured by the normalized Doppler offset and bandwidth. Below, we examine whether the Doppler spectra of sea clutter possess the bi-phase property like texture. For the sea clutter data in Fig. 1(b) at dwelling mode, the normalized Doppler offset f_d and bandwidth σ_d of sea clutter time series with the duration of 0.1 s are calculated from the Doppler power spectrum by

$$f_d = \frac{1}{a} \sum_{k=-K/2}^{K/2-1} \frac{k}{K} \mathrm{DPS}(k),$$

$$\sigma_d = \sqrt{\frac{1}{a} \sum_{k=-K/2}^{K/2-1} \left(\frac{k}{K} - f_d\right)^2 \mathrm{DPS}(k)}$$

$$a = \sum_{k=-K/2}^{K/2-1} \mathrm{DPS}(k),$$

$$\mathrm{DPS}(k) = \left|\mathrm{DFT}\left([c(1), c(2), \ldots, c(K)]\right)\right|^2$$
$$k = -K/2, \ldots, K/2 - 1. \tag{2}$$

where the "DFT" denotes the discrete Fourier transform. Within the short duration of 0.1 s, the texture is a positive random constant [34], and thus normalized Doppler offset and bandwidth are determined by speckle. Each bright or dim region is at least three seconds and contains at least 30 samples of the normalized Doppler offset and bandwidth. Then average Doppler offset and bandwidth are calculated to characterize the spectral shape of each region. Sporadic abnormal samples are removed in calculation to eliminate the effects of abnormal events such as burst scattering. Fig. 3(a) and (b) reveals the difference of the average Doppler offsets and bandwidths of the six bright regions and six dim regions. The spectral shapes are comparable in bright regions or dim regions, and the bright regions have larger Doppler offsets and smaller Doppler bandwidths than the dim regions. Therefore, the Doppler spectral shapes also exhibit the bi-phase property like texture. Other datasets have similar behavior in texture and Doppler spectral shape.

From the analysis above, a remarkable characteristic of long-wave modulated sea clutter is the dependency of the bi-phase variations of texture and Doppler spectrum. This dependency can be observed in many measured databases and has been analyzed by some researchers. The bi-phase variation of texture leads to the bi-phase property of intensity and amplitude distributions of sea clutter. At low grazing angles, the Doppler spectra of dim regions exhibit larger bandwidths and smaller offsets in the field measurements [17] and numerical simulations [22], partly owing to the shadowing effect. At medium or high-grazing angles, Doppler offsets of sea clutter are positively correlated with amplitude. Doppler spectra of sea clutter in high-intensity regions have broadening shapes and even bimodal behavior, which is observed in the wave tanks [39], field experiments [23], and numerical simulations [24], partly owing to the effect of breaking waves at wave crests.

C. Bi-Phase Compound-Gaussian Mixture Model

Based on the bi-phase behaviors of both texture and Doppler spectrum, a BP-CGMM is proposed to characterize long-wave modulated sea clutter. The BP-CGMM is defined as follows.

Let $\mathbf{r}$ denote the coordinate of each resolution cell, Ω denote the universal set of $\mathbf{r}$ in a patch of sea surface, and $\mathbf{z_r}$ denote the sea clutter vector at the resolution cell $\mathbf{r}$. Specially, the coordinate of each resolution cell is always a vector which denotes its location on a 2-D plane, namely, range-time plane at dwelling mode or range-azimuth plane at scan mode. In the BP-CGMM, the resolution cells in Ω can be grouped into two disjoint sets, the dim region Ω_0 and bright region Ω_1

$$\mathbf{z_r} = \begin{cases} \sqrt{\tau_0(\mathbf{r})}\mathbf{u}_0(\mathbf{r}), \mathbf{r} \in \Omega_0 \\ \sqrt{\tau_1(\mathbf{r})}\mathbf{u}_1(\mathbf{r}), \mathbf{r} \in \Omega_1 \end{cases}, \text{where} \begin{cases} \Omega_0 \cap \Omega_1 = \emptyset \\ \Omega_0 \cup \Omega_1 = \Omega \end{cases} \tag{3}$$
$$\mathbf{u}_0(\mathbf{r}) \sim \mathbb{CN}(\mathbf{0}, \mathbf{M}_0), \mathbf{u}_1(\mathbf{r}) \sim \mathbb{CN}(\mathbf{0}, \mathbf{M}_1)$$

where $\mathbb{CN}(\mathbf{0}, \mathbf{M})$ denotes the complex Gaussian random vector with zero mean and covariance matrix $\mathbf{M}$, namely, speckle covariance matrix in the CGM. Moreover, the textures τ_0, τ_1 and speckle vectors $\mathbf{u}_0, \mathbf{u}_1$ in the two regions satisfy:
1) textures and speckle vectors in the two regions are independent of each other;
2) in each region, textures follow the same distribution;
3) in each region, speckle vectors at adjacent resolution cells share the same covariance matrix.

The third term implies that the speckle covariance matrices of two adjacent cells in different regions are probably quite different. For radars operating at the scan mode, resolution cell $\mathbf{r}$ is located on the range-azimuth plane, where textures reflect the underlying gravity-wave-induced amplitude variation and are sensitive to the variation of sea states and viewing geometry of radar, including the grazing angle and the wave direction. For instance, the shadowing proportion of sea surface at a beam position is a function of the grazing angle [40] which affects the mixture ratio of the two regions in the BP-CGMM. Thus, the BP-CGMM is suitable for a small patch of sea surface, where sea states and the viewing geometry of the radar have ignorable differences. Similarly, for radars operating at the dwelling mode, the BP-CGMM is suitable for the radar data within a short radial scope.

Different from the existing mixture models whose textures are characterized by bimodal pdfs [18], [19], the proposed

BP-CGMM compromises the requirement of subtle characterization and mathematical tractability in modeling the long-wave modulated sea clutter by applying further physical investigation. The resolution cells in a patch of sea surface are spatially grouped into two sets to characterize the bi-phase property of sea clutter in amplitude distribution and Doppler spectrum. Viewing excellent modeling performance of the inverse Gamma-distributed textures on heavy-tailed sea clutter data [12], the BP-CGMM employs the inverse Gamma distributions to model the textures in the two sets, and thus the model is specified by five parameters, two scale parameters η_0 and η_1, two shape parameters λ_0 and λ_1, and a mixture ratio $\alpha \in [0,1]$

$$f_{\alpha,\eta_0,\lambda_0,\eta_1,\lambda_1}(z) = \frac{2\alpha\lambda_0 z}{\eta_0(\lambda_0-1)\left(1+\frac{z^2}{\eta_0(\lambda_0-1)}\right)^{\lambda_0+1}}$$
$$+ \frac{2(1-\alpha)\lambda_1 z}{\eta_1(\lambda_1-1)\left(1+\frac{z^2}{\eta_1(\lambda_1-1)}\right)^{\lambda_1+1}}$$

$$F_{\alpha,\eta_0,\lambda_0,\eta_1,\lambda_1}(z) = 1 - \frac{\alpha}{\left(1+\frac{z^2}{\eta_0(\lambda_0-1)}\right)^{\lambda_0}} - \frac{1-\alpha}{\left(1+\frac{z^2}{\eta_1(\lambda_1-1)}\right)^{\lambda_1}}$$

$$\eta_0,\eta_1 > 0, \lambda_0,\lambda_1 > 1, \alpha \in [0,1] \tag{4}$$

where z denotes the amplitude of sea clutter, the scale parameters η_0 and η_1 equal to the average intensity of sea clutter in the dim region and the bright region, and the shape parameters λ_0 and λ_1 reflect the non-Gaussianity of sea clutter, the f and F denote the pdf and CDF of the amplitude of sea clutter, separately. The shape parameters are restricted to be larger than one to assure the existence of mean intensity of sea clutter, which follows physical reality [12]. The mixture ratio α is substantially the percentage of the resolution cells in the dim region and is also an unknown parameter to be estimated from data. Particularly, as the mixture ratio tends to zero or one, the BP-CGMM degenerates to the commonly used CGM.

In what follows, we investigate the parameter estimation of the BP-CGMM. The fitting of the empirical CDF (ECDF) of data is a commonly used method in parameter estimation [41]. By minimizing the mean square error between the parametric CDF and the ECDF of the data, the five parameters of the BP-CGMM are estimated by solving the optimization

$$\min_{\substack{\alpha \in [0,1], \\ \eta_0,\eta_1 > 0; \lambda_0,\lambda_1 > 1}} \left\{ \sum_n \left| F_{\alpha,\lambda_0,\eta_0,\lambda_1,\eta_1}(z_n) - \text{ECDF}(z_n) \right|^2 \right\} \tag{5}$$

where z_n are the sampling points in the ECDF of the data. In practice, measured data contain a small number of outliers with large amplitudes. In this case, the ECDF of the data is replaced by the truncated version with several percentages of the largest amplitude samples deleted from the data to obtain outlier-robust estimates [42]. For comparison, the two parameters of the CGM with inverse Gamma texture are also estimated by the same method.

Here, 75 datasets of sea clutter at the dwelling mode in the CSIR database [31] are used to validate the BP-CGMM. Each dataset covers a narrow range scope, where the grazing angle has

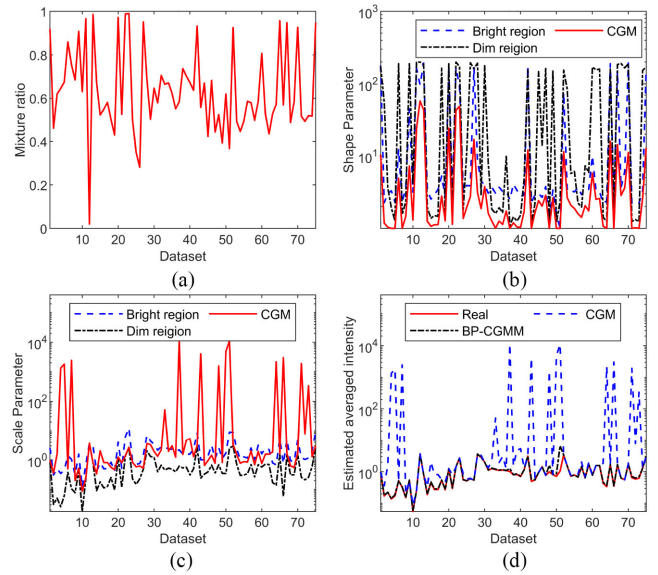| Parameter	Range
Grazing angle	0.26°-1.66°
Wave direction	0.18°-64.71°
Wind direction	13.49°-179.83°
Wind speed	1.89-9.40 m/s
Significant wave height	2.09-3.52 m
Sea State (Beaufort scale)	2-5

Fig. 4.   Estimated parameters of the 75 datasets in the BP-CGMM and CGM. (a) Mixture ratios. (b) Shape parameters. (c) Scale parameters. (d) Estimated averaged intensities.

only a small change, and the sea state keeps invariant. Thus, sea clutter in each dataset can be regarded to follow a single CGM or BP-CGMM. Owing to sufficient samples in each dataset, the ECDF from the data is of high precision, and the fitting method in (5) can work well. Table II lists the dynamic ranges of the viewing geometry and environmental parameters of the 75 datasets, which are rather various and enough to validate the fitting performance of the BP-CGMM. For convenience in analysis of the influence of sea states, the 75 datasets are labeled by arranging in terms of the significant wave height (SWH) from lowest to highest. Fig. 4(a) plots the mixture ratios of the 75 datasets under BP-CGMM. It is found that in low sea states, the mixture ratio is close to zero or one, which means that the BP-CGMM degenerates to the CGM as the bi-phase property of sea clutter is not evident in low sea states. Moreover, the mixture ratios of most of the datasets are greater than 0.5, which can be interpreted from the time ratio of the crests to troughs of long waves on the sea surface. Fig. 4(b) plots the shape parameters of the bright region and dim region in the BP-CGMM and the shape parameters in the CGM of the 75 datasets. A common phenomenon is that the two shape parameters of the BP-CGMM

are always larger than the shape parameter of the CGM. It is known that a smaller shape parameter means a heavier tail of the amplitude distribution. Because of the model mismatch of the CGM, the amplitude difference between the bright region and dim region in the BP-CGMM is wrongly owed to the tail of the distribution in the CGM. Moreover, it is also found that for about half of the datasets the shape parameter of the dim region is quite large, meaning that sea clutter in the dim region of these datasets is close to Gaussian clutter.

Fig. 4(c) plots estimated scale parameters of the 75 datasets of the BP-CGMM and CGM. For the BP-CGMM, the estimated scale parameters of bright regions are always larger than that of dim regions, which results from the different scattering mechanisms in the two regions. The estimated scale parameters of the CGM distinctly deviate from the two estimated scale parameters of the BP-CGMM in some datasets, especially in high sea states. In general, the estimated scale parameter of the CGM is between the two estimated scale parameters of the BP-CGMM in one dataset. A few exceptions in Fig. 4(c) might result from estimation errors. The source of the errors is analyzed by comparing the average intensity estimated directly from the data and the estimated average intensity calculated from the estimated parameters of the BP-CGMM or CGM. The scale parameter in the CGM indicates the average intensity of sea clutter. In the BP-CGMM, the average intensity of sea clutter is the weighted sum of the two scale parameters

$$\bar{p}_{\text{BP-CGMM}} = \hat{\alpha}\hat{\eta}_0 + (1 - \hat{\alpha})\hat{\eta}_1. \tag{6}$$

Fig. 4(d) plots the average intensities of the datasets, the estimated scale parameters of the CGM, and the estimated average intensities under the BP-CGMM by (6). It can be observed that the estimates from (6) highly accord with the average intensities of the data in all datasets. However, the estimations in the CGM severely deviate from the average intensities of the data in many datasets. These overestimates substantially result from model mismatch of the CGM to characterize long-wave modulated sea clutter.

To quantitatively assess the goodness-of-fit of the CGM and BP-CGMM to sea clutter, the Bhattacharyya distance [43] and Log-Kolmogorov–Smirnoff (Log-K-S) distance [44] are used to measure their fitting performance. In the BP-CGMM, the two distances are computed by

$$d_B \left(\text{Epdf}, \hat{\alpha}, \hat{\eta}_0, \hat{\lambda}_0, \hat{\eta}_1, \hat{\lambda}_1 \right)$$
$$= -\ln \left(\sum_{n=1}^{N} \sqrt{\text{Epdf}(z_n) f_{\hat{\alpha}, \hat{\eta}_0, \hat{\lambda}_0, \hat{\eta}_1, \hat{\lambda}_1}(z_n)} \right)$$
$$d_{Log-K-S} \left(ECDF, \hat{\alpha}, \hat{\eta}_0, \hat{\lambda}_0, \hat{\eta}_1, \hat{\lambda}_1 \right)$$
$$= \frac{1}{N} \sum_{n=1}^{N} \left| \ln \left(\frac{1 - F_{\hat{\alpha}, \hat{\eta}_0, \hat{\lambda}_0, \hat{\eta}_1, \hat{\lambda}_1}(z_n)}{1 - \text{ECDF}(z_n)} \right) \right| \tag{7}$$

where N is the number of the sample points, Epdf is the empirical pdf of the data. The Bhattacharyya distance reflects the total similarity of the Epdf and fitting pdf of the BP-CGMM, and the Log-K-S distance emphasizes the goodness-of-fit of the tails of
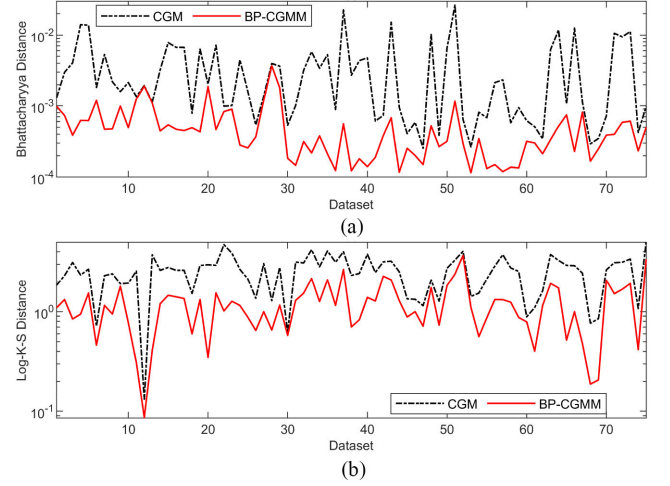

Fig. 5. Comparison of fitting performance of the CGM and BP-CGMM on the 75 datasets. (a) Bhattacharyya distance. (b) Log-K-S distances.
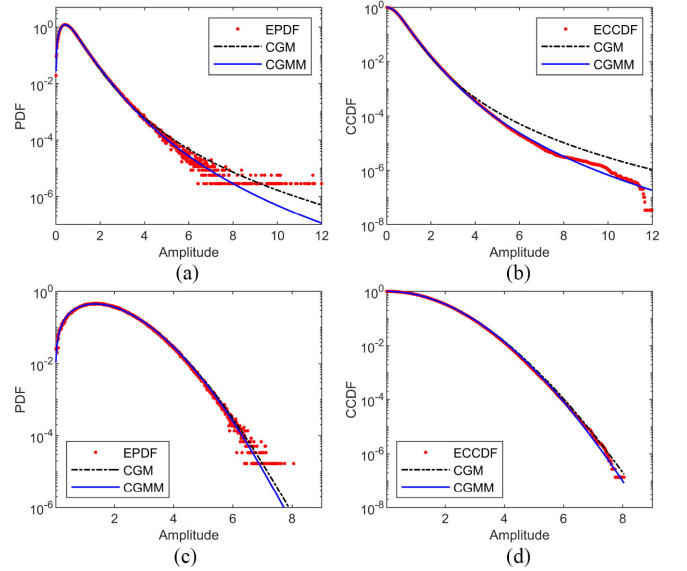

Fig. 6. Epdf and ECCDF fitting results of the two typical datasets in the BP-CGMM and CGM. (a) Epdf fitting result at sea state 5. (b) ECCDF fitting result at sea state 5. (c) Epdf fitting result at sea state 2. (d) ECCDF fitting result at sea state 2.

the ECDF and fitting CDF. Fig. 5 illustrates the Bhattacharyya distances and Log-K-S distances of the 75 datasets under the BP-CGMM and CGM. The two distances under the BP-CGMM are always smaller than that under the CGM in all the 75 datasets. Therefore, the BP-CGMM can better fit the main body of Epdf and the tail of ECDF of every dataset than the CGM does. The CGM fails to characterize distinct statistical characteristics in bright region and dim region due to its unimodal nature.

To illustrate the fitting performance of the BP-CGMM and CGM, the fitting curves of two typical datasets separately in high sea state and low sea state are plotted in Fig. 6, the estimated parameters are listed in Table III, and the fitting errors are listed in Table IV. Fig. 6(a) and (b) demonstrates the fitting results

TABLE III
ESTIMATED PARAMETERS OF THE BP-CGMM AND CGM IN THE TWO
DATASETS

Parameter	CFC16-006	CFA18-003
$\hat{\alpha}$	0.49	0.02
$\hat{\eta}_0$	0.31	3.67
$\hat{\lambda}_0$	190.81	199.73
$\hat{\eta}_1$	0.94	3.69
$\hat{\lambda}_1$	3.63	97.00
$\hat{\eta}$	0.63	3.70
$\hat{\lambda}$	2.85	58.14

TABLE IV
FITTING ERRORS OF THE BP-CGMM AND CGM IN THE TWO DATASETS

Dataset	Measurement	CGM	BP-CGMM
CFC16-006	d_B	2.93×10^{-4}	1.68×10^{-4}
	$d_{Log\text{-}K\text{-}S}$	7.66×10^{-1}	1.88×10^{-1}
CFA18-003	d_B	1.32×10^{-1}	8.63×10^{-2}
	$d_{Log\text{-}K\text{-}S}$	1.95×10^{-3}	1.91×10^{-3}

of the Epdf and empirical complementary CDF (ECCDF) of the dataset "CFC16-006" in sea state 5. Both the BP-CGMM and CGM attain satisfactory fitting performance at the main body of Epdf and ECCDF. Nevertheless, the fitting curves of the two models exhibit evident deviations at the tails of Epdf and ECCDF. The fitting of the tails is vital to control false alarm rates in target detection. According to Fig. 6(b), Tables III and IV, the fitting result of the CGM has a heavier tail, smaller shape parameter, and larger fitting errors of the Epdf and ECCDF than the BP-CGMM does. Based on the bi-phase property, two CGMs in the BP-CGMM separately characterize sea clutter in the bright region and dim region. As listed in Table III, the two CGMs have distinct scale and shape parameters and thus, attain better fitting performance of the Epdf and ECCDF of the data. Fig. 6(c) and (d) demonstrates the fitting results of Epdf and ECCDF of the dataset "CFA18-003" in sea state 2. The fitting curves of the BP-CGMM and CGM exhibit similar behaviors. In Table III, the mixture ratio of the BP-CGMM is close to zeros, which implies that the bi-phase property of sea clutter is not evident, and the dataset can be modeled by the unimodal CGM model. In Table IV, the results show that both the BP-CGMM and CGM can fit the main body of the Epdf and the tail of the ECCDF of the data with minor errors, although the result of the BP-CGMM is a little better than that of the CGM. Therefore, we conclude that the BP-CGMM is necessary in moderate and high sea states and is an alternative in low sea states for long-wave modulated high-resolution sea clutter in comparison with the CGM.

III. SCENE-SEGMENTATION-BASED TARGET DETECTION UNDER BP-CGMM

Under the CGM of sea clutter, target detection is performed by the standard flowchart of the model parameter estimation of

sea clutter in advance, followed by adaptive coherent detection at individual spatial resolution cells [11]–[13]. Under the BP-CGMM, the resolution cells of the scene need to be grouped into two sets before detection based on the cached data, which is referred to as scene-segmentation. Due to the data caching, the cell-by-cell test with a time delay of several milliseconds is replaced by the batch test with a larger time delay. The large time delay is often unacceptable for air surveillance radars that focus on high-velocity targets whose velocities are probably several hundreds of meters per second. Whereas, it is tolerable for surface surveillance radars that focus on sea-surface targets whose velocities are usually below 30 meters per second (60 knots) [32]. For example, when a surface surveillance radar scans at 6 rotations per minute and the whole scene is separated into 12 sections for the batch test, each section takes up 30 degrees in azimuth and brings a time delay less than one second of batch test which is allowable for sea-surface target tracking in surface surveillance radars. When surface surveillance radars work at the dwelling mode, it is practical that the radar returns can be cached for several subseconds for scene-segmentation and batch test. Therefore, we present a target detection scheme for surface surveillance radars based on the BP-CGMM of sea clutter and batch test. The flowchart is shown in Fig. 7. The first block is the *data caching* by which the returns in a section or time interval of several subseconds are collected for scene segmentation. The next block is the *data preprocessing* which splits the cached data into batches with appropriate azimuth coverage and range scope for scan mode or batches with proper range scope for dwelling mode. And then, the five parameters of the BP-CGMM are estimated from the data batch. The third block is the *scene segmentation* based on the Bayes rule to group the resolution cells in the batch into two sets, which is given in detail in sequent Section III-A. The fourth block is the *morphological correction* of the scene segmentation to correct some wrongly classified cells, particularly target cells in the dim region, which is also given in Section III-A. The last block is the *adaptive coherent detection* on the segmented scene, which forms the main content of Section III-B.

A. Scene Segmentation Based on Bayes Rule and Morphological Filter

In a range-azimuth scene or a range-time scene, the returns can be expressed by

$$\mathbf{z}_\mathbf{r} = [z_\mathbf{r}(1), z_\mathbf{r}(2), \ldots, z_\mathbf{r}(M)]^T, \mathbf{r} \in \Omega \qquad (8)$$

where the bold font $\mathbf{r}$ denotes the resolution cell in the scene, and an M-dimensional complex vector represents the returns at each resolution cell. In terms of the parameter estimates of the BP-CGMM, the prior probability of a resolution cell to fall into the dim region Ω_0 is $\hat{\alpha}$ and the prior probability of it to fall into the bright region Ω_1 is $1 - \hat{\alpha}$. The conditional pdf of the complex vector $\mathbf{z}_\mathbf{r}$ in $\mathbf{r} \in \Omega_0$ is the compound-Gaussian distribution whose texture component is determined by scale and shape parameters $\hat{\eta}_0$ and $\hat{\lambda}_0$, and speckle component is determined by unknown and varying speckle covariance matrix $\mathbf{M}$. When $\mathbf{r} \in \Omega_1$, the conditional pdf is similar except for different scale and shape
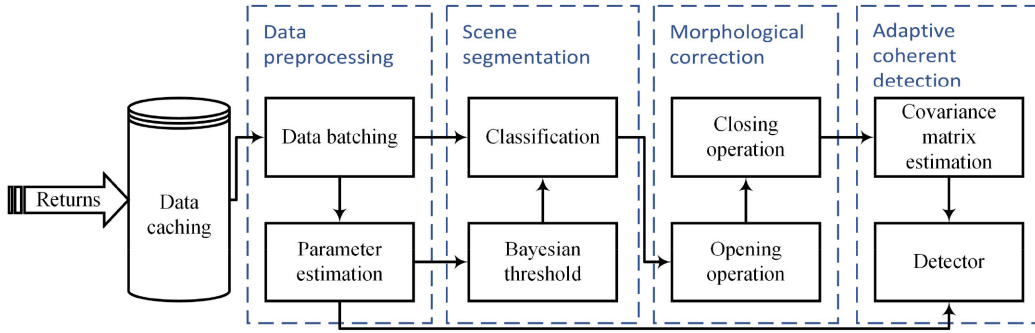
Fig. 7   Flowchart of the scene-segmentation-based target detection scheme in the BP-CGMM of sea clutter.

parameters. Because the bi-phase variation of both the texture and Doppler spectrum are consistent, scene segmentation is based on the texture.

In the BP-CGMM, the textures in the two regions both follow the inverse Gamma distribution

$$p\left(\tau\,|\Omega_0\right) = \frac{\left((\hat{\lambda}_0 - 1)\hat{\eta}_0\right)^{\hat{\lambda}_0}}{\Gamma(\hat{\lambda}_0)\tau^{(\hat{\lambda}_0+1)}} \exp\left(-\frac{\left(\hat{\lambda}_0 - 1\right)\hat{\eta}_0}{\tau}\right)$$

$$p\left(\tau\,|\Omega_1\right) = \frac{\left((\hat{\lambda}_1 - 1)\hat{\eta}_1\right)^{\hat{\lambda}_1}}{\Gamma(\hat{\lambda}_1)\tau^{(\hat{\lambda}_1+1)}} \exp\left(-\frac{\left(\hat{\lambda}_1 - 1\right)\hat{\eta}_1}{\tau}\right). \quad (9)$$

Based on the Bayes rule, the optimal threshold T_{OBT} is calculated by minimizing the total error probability

$$T = \arg\min_{T_{\text{OBT}}>0}\left\{\hat{\alpha}\int_{T_{\text{OBT}}}^{+\infty} p\left(\tau\,|\Omega_0\right)d\tau\right.$$
$$\left. + (1 - \hat{\alpha})\int_{0}^{T_{\text{OBT}}} p\left(\tau\,|\Omega_1\right)d\tau\right\}. \quad (10)$$

If the distribution parameters are known, the optimization problem in (10) can be simplified by the minimum Bayesian risk rule with a threshold based on the prior probabilities of the two hypotheses [28]

$$\frac{p\left(\tau|\Omega_1\right)}{p\left(\tau|\Omega_0\right)}\mathop{\gtrless}_{\Omega_0}^{\Omega_1}\frac{\alpha}{1 - \alpha}. \quad (11)$$

In real clutter environments, the texture or intensity of sea clutter at each cell is unknown and needs to be estimated from radar returns. Replacing the true values of texture and distribution parameters in (11) with their estimates yields a cell-level segmentation of the scene

$$\tilde{\Omega}_0 = \left\{\mathbf{r} \in \Omega : \frac{p\left(\hat{\tau}|\Omega_1\right)}{p\left(\hat{\tau}|\Omega_0\right)} < \frac{\hat{\alpha}}{1 - \hat{\alpha}}\right\},$$

$$\tilde{\Omega}_1 = \left\{\mathbf{r} \in \Omega : \frac{p\left(\hat{\tau}|\Omega_1\right)}{p\left(\hat{\tau}|\Omega_0\right)} \geq \frac{\hat{\alpha}}{1 - \hat{\alpha}}\right\}. \quad (12)$$

In the cell-level segmentation, the simple thresholding segmentation results in small holes or short cracks in the bright region and dim region. Particularly, target returns, which have high intensity at the cells occupied by a target, yield large

estimates of the texture. These large values form small holes in the dim region at the scan mode and short cracks in the dim region at the dwelling mode. Because the bright region and dim region are related to the crests and troughs of long waves on the sea surface, scene segmentation is substantially region level. Note that the cell-level segmentation in (12) is a binary image $\tilde{\chi}$, where the cells of the value of one form $\tilde{\Omega}_1$ and the cells of the value of zero form $\tilde{\Omega}_0$. Thus, the opening operator in the mathematical morphology is first used in the binary image to eliminate the effect of target returns, which is implemented by the series of two linear filters followed by a logical operator

$$f_{\text{erosion}}(\mathbf{r}) = \left\{\tilde{\chi} * S(\mathbf{r}) = \sum_{\mathbf{r}} S(\mathbf{r})\right\},$$
$$f_{\text{opening}}(\mathbf{r}) = \{f_{\text{erosion}} * S(\mathbf{r}) > 0\} \quad (13)$$

where S is the structural element of the morphological operator and can be a two-dimensional filter whose coefficients are zero or one. Then the logical operator after the morphological filtering in (13) is given by

$$\bar{\Omega}_0 = \{\mathbf{r} \in \Omega : f_{\text{opening}}(\mathbf{r}) = 0\},$$
$$\bar{\Omega}_1 = \{\mathbf{r} \in \Omega : f_{\text{opening}}(\mathbf{r}) = 1\}. \quad (14)$$

After the morphological filtering of (13), the bright region does not contain any separate cluster whose size is smaller than that of the structuring element. However, the bright region probably contains small holes or short cracks consisting of dim cells. Based on $\bar{\Omega}_0$ and $\bar{\Omega}_1$, the binary image is defined by $\bar{\chi}$. These small holes or short cracks in the bright region can be removed by applying the closing operator on $\bar{\chi}$

$$g_{\text{dilation}}(\mathbf{r}) = \{\bar{\chi} * S(\mathbf{r}) > 0\},$$

$$g_{\text{closing}}(\mathbf{r}) = \left\{g_{\text{dilation}} * S(\mathbf{r}) = \sum_{\mathbf{r}} S(\mathbf{r})\right\}$$

$$\hat{\Omega}_0 = \{\mathbf{r} \in \Omega : g_{\text{closing}}(\mathbf{r}) = 0\},$$
$$\hat{\Omega}_1 = \{\mathbf{r} \in \Omega : g_{\text{closing}}(\mathbf{r}) = 1\}. \quad (15)$$

In this way, all the resolution cells in the scene are classified into the bright and dim regions based on the BP-CGMM and proximity relation of cells. Fig. 8 illustrates the complete process of the scene segmentation. Fig. 8(a) is the estimates of the texture
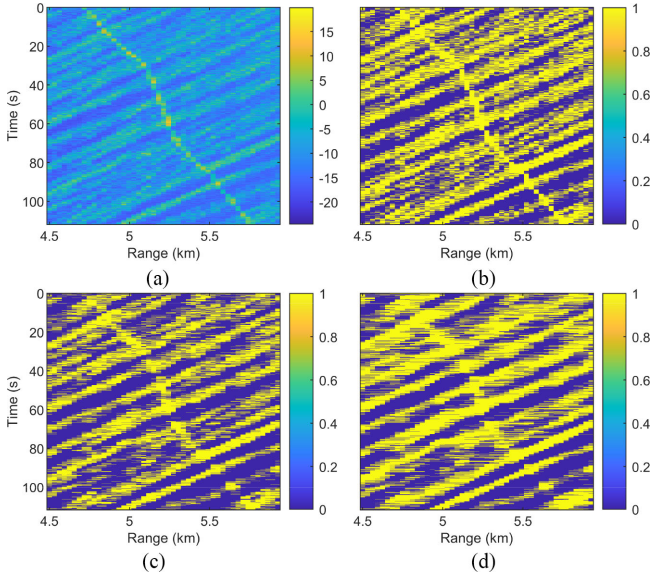
Fig. 8. Illustration of the scene segmentation of a measured dataset. (a) Estimation of texture. (b) Result of Bayesian threshold segmentation. (c) Result after opening operation. (d) Result after closing operation.

on the plane of radial distance versus scan time. There is a trace of a sea-surface moving target in the scene to verify the robustness of the segmentation method. Fig. 8(b) is the cell-level segmentation, where the target trace in the dim region is falsely classified into the bright region. Fig. 8(c) is the result after the opening operation on the cell-level segmentation. The false classification of the target trace in the dim region is corrected by filling small holes and short cracks in the dim region. Fig. 8(d) plots the result after the closing operation, where a region-based scene segmentation is obtained.

B. Scene-Segmentation-Based Adaptive Detection Under BP-CGMM

In the segmented scene, sea clutter vectors in the dim region follow the SIRV model with the inverse Gamma-distributed texture of the scale and shape parameters $\hat{\eta}_0, \hat{\lambda}_0$, and sea clutter in the bright region follows that of the scale and shape parameter $\hat{\eta}_1, \hat{\lambda}_1$. In the SIRV model with the inverse Gamma texture, the optimal coherent detector is the GLRT-LTD [14], and its adaptive version is applied to the resolution cell in the bright region or dim region (16) shown at the bottom of this page, where $\mathbf{p}(f_d)$ is the Doppler steering vector, $\hat{\mathbf{M}}$ is the estimated speckle covariance matrix from P RCs, the hypothesis H_1 means target presence,

and the hypothesis H_0 means target absence at the Doppler bin. A CUT is affirmed to target presence if there is one Doppler bin declaring that the hypothesis H_1 holds. The decision threshold is determined by the number M of integrated pulses, the number P of the RCs, the shape parameter, and the desired false alarm rate P_{fa}. It is known that the GLRT-LTD is of constant false alarm rate (CFAR) with respect to the number M of integrated pulses, the speckle covariance matrix, the scale parameter and the Doppler steering vector, and the decision threshold can be analytically given [12]. For the adaptive version, the decision threshold fails to be analytically given and can be obtained from the Monte-Carlo test using simulated data [11], [13]. In (16), the bright and dim regions use different decision thresholds matching the shape parameter of sea clutter in the region to assure the CFAR in the whole scene.

In the BP-CGMM, the selection of RCs to estimate the speckle covariance matrix is an essential factor to influence the detection performance. Because the bi-phase property of the Doppler spectra of sea clutter is consistent with that of the texture, only adjacent cells in the bright region or the dim region share the same speckle covariance matrix. Whereas, one cell in the bright region and one cell in the dim region probably have quite different speckle covariance matrices, though they are close to each other. Thus, the RCs of a CUT are selected by

$$\forall \mathbf{r} \in \hat{\Omega}_i,$$

$$\Lambda(\mathbf{r}) = \left\{ \begin{array}{l} \mathbf{r}_1, \mathbf{r}_2, \cdots, \mathbf{r}_P \in \hat{\Omega}_i : \text{Cells in the same beam} \\ \qquad\qquad\qquad\text{position and closest to the CUT } \mathbf{r} \end{array} \right\},$$

$$i = 0, 1. \qquad (17)$$

The speckle covariance matrix is estimated by the normalized sample covariance matrix [15]

$$\hat{\mathbf{M}} = \frac{1}{P} \sum_{\mathbf{r}' \in \Lambda(\mathbf{r})} \frac{\mathbf{z}_{\mathbf{r}'} \mathbf{z}_{\mathbf{r}'}^H}{\mathbf{z}_{\mathbf{r}'}^H \mathbf{z}_{\mathbf{r}'}}. \qquad (18)$$

which can also be replaced by other effective estimators [45].

IV. EXPERIMENTAL RESULTS ON MEASURED DATA AND PERFORMANCE COMPARISON

Two datasets "TFC15-025" and "TFA17-001" from the CSIR database are used to test the validity and robustness of the scene-segmentation-based detection method under the BP-CGMM. The two datasets were collected in different radar and environmental parameters, and the main parameters are listed in Table V. The test target in the first dataset is a rigid inflatable boat with an average SCR of 6.3 dB and sailed away from radar

$$\forall \mathbf{r} \in \hat{\Omega}_i, \xi_i(f_d, \mathbf{r}) \equiv$$

$$\frac{\left| \mathbf{p}^H(f_d) \hat{\mathbf{M}}^{-1} \mathbf{z}_{\mathbf{r}} \right|^2}{(\mathbf{p}^H(f_d) \hat{\mathbf{M}}^{-1} \mathbf{p}(f_d))(\hat{\eta}_i(\hat{\lambda}_i - 1) + \mathbf{z}_{\mathbf{r}}^H \hat{\mathbf{M}}^{-1} \mathbf{z}_{\mathbf{r}})} \underset{H_0}{\overset{H_1}{\gtrless}} \text{Threshold}(P, M, \hat{\lambda}_i, P_{fa})$$

$$i = 0, 1 \qquad\qquad (16)$$

TABLE V
MAIN PARAMETERS OF THE TWO DATASETS

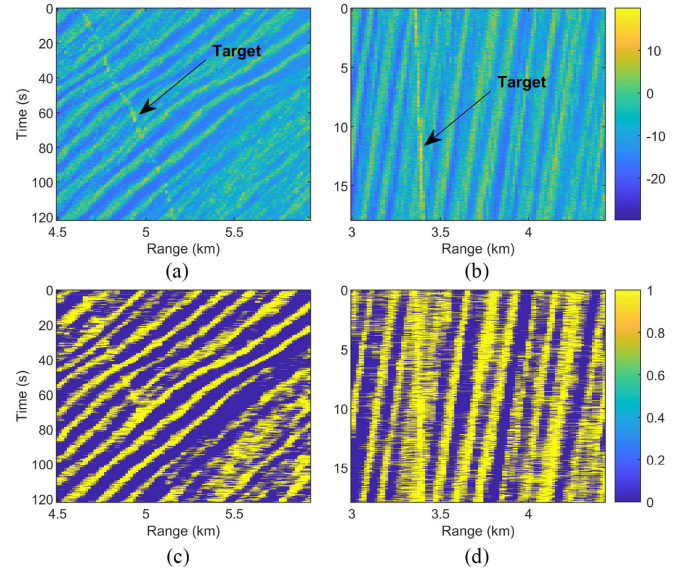| Parameter	TFC15-025	TFA17-001
PRF	2.5 kHz	5 kHz
Tx. frequency	9 GHz	6.9 GHz
Antenna elevation	-1.2°	-0.9°
Antenna bandwidth	1.8°	2°
Range	4500 m-5940 m	3001 m-4441 m
Tx. bandwidth	10 MHz	10 MHz
Wind direction	14.8°	88.5°
Wave period	11 s	14 s
SWH	2.87 m	2.26 m
Sea state (Beaufort scale)	5	4
Test target	Rigid inflatable boat	Fishing boat
$\hat{\alpha}$	0.57	0.41
$\hat{\eta}_0$	0.57	1.13
$\hat{\lambda}_0$	2.53	2.14
$\hat{\eta}_1$	0.07	0.11
$\hat{\lambda}_1$	2.20	2.81
$\hat{\eta}$	1.21	2.97
$\hat{\lambda}$	1.07	1.11

Fig. 9. Intensity in decibel and region-based scene segmentation of two datasets. (a) Intensity of the first dataset. (b) Intensity of the second dataset. (c) Region-level scene segmentation of the first dataset. (d) Region-level scene segmentation of the second dataset, where the arrows mark the traces of the test targets.

with a radial velocity range of [1, 8.5] m/s in sea state 5. The test target in the second dataset is a fishing boat with an average SCR of 7.9 dB and sailed away from radar with a radial velocity range of [1.2, 3] m/s in sea state 4. The power maps of the two datasets are plotted in Fig. 9(a) and (b), and their region-level scene segmentations are illustrated in Fig. 9(c) and (d).

To verify the performance of the scene-segmentation-based GLRT-LTD, it is compared with the GLRT-LTD under the CGM with the inverse Gamma-distributed texture and the scene-segmentation-based GLRT-LTD only using the bi-phase property of the amplitude distribution in the two datasets. When the bi-phase property of Doppler spectra of sea clutter is not considered, the RCs of a CUT are selected from the whole scene by the proximity criterion

$$\forall \mathbf{r} \in \Omega, \bar{\Lambda}(\mathbf{r})$$

$$= \left\{ \begin{array}{l} \mathbf{r}_1, \mathbf{r}_2, \cdots, \mathbf{r}_P \in \Omega : \text{Cells in the same beam} \\ \qquad\qquad\qquad \text{position and closest to the CUT } \mathbf{r} \end{array} \right\}. \quad (19)$$

For convenience, the scene-segmentation-based GLRT-LTD using (16) and (17) is denoted by the adaptive full-scene-segmentation-based GLRT-LTD (FSS-GLRT-LTD), where the word "full" means the usage of the bi-phase properties of both amplitude distribution and Doppler spectrum. The one using (16) and (19) is referred to as the adaptive half-scene-segmentation-based GLRT-LTD (HSS-GLRT-LTD), where the word "half" means the usage of only the bi-phase property of the amplitude

distribution. When the CGM with inverse Gamma distributed texture is used to model the two datasets, the scale and shape parameters are [1.21, 1.07] and [2.97, 1.11], respectively. The shape parameters of the CGMs are much smaller than that of the BP-CGMMs. Due to the model mismatch, the average intensity difference in the bright region and dim region is mistakenly regarded as the contribution of the heavy tail of the amplitude distribution of sea clutter. Under the CGM, the adaptive GLRT-LTD [12] is implemented by (20) shown at the bottom of this page, where the speckle covariance matrix is estimated by terms of (18) and (19).

In detection, the number of integrated pulses is $M = 8$, the number of RCs is set as $P = 24$, and the 32 uniform Doppler bins are used to search the Doppler steering vector of the unknown target. In other words, the decision on each range-time cell $\mathbf{r}$ is based on the largest statistics of all Doppler bins

$$\varsigma_{\text{GLRT-LTD}}(\mathbf{r}) = \max_{f_d} \left\{ \xi_{\text{GLRT-LTD}}(f_d, \mathbf{r}) \right\}$$

$$\varsigma_{\text{FSS-GLRT-LTD}}(\mathbf{r}) = \left\{ \begin{array}{ll} \max_{f_d} \left\{ \xi_0(f_d, \mathbf{r}) \right\}, \mathbf{r} \in \hat{\Omega}_0 \\ \max_{f_d} \left\{ \xi_1(f_d, \mathbf{r}) \right\}, \mathbf{r} \in \hat{\Omega}_1. \end{array} \right. \quad (21)$$

The test statistics of the HSS-GLRT-LTD at one range-time cell $\mathbf{r}$ have the same form as that of the FSS-GLRT-LTD, except that the RCs are selected by terms of (19) instead of (17). Fig. 10(a) and (d) plots the values of the test statistic of the

$$\xi_{\text{GLRT-LTD}}(f_d, \mathbf{r}) \equiv$$

$$\frac{\left| \mathbf{p}^H(f_d) \hat{\mathbf{M}}^{-1} \mathbf{z}_\mathbf{r} \right|^2}{(\mathbf{p}^H(f_d) \hat{\mathbf{M}}^{-1} \mathbf{p}(f_d))(\hat{\eta}(\hat{\lambda} - 1) + \mathbf{z}_\mathbf{r}^H \hat{\mathbf{M}}^{-1} \mathbf{z}_\mathbf{r})} \underset{H_0}{\overset{H_1}{\underset{<}{>}}} \text{Threshold}(P, M, \hat{\lambda}, P_{fa}) \quad (20)$$
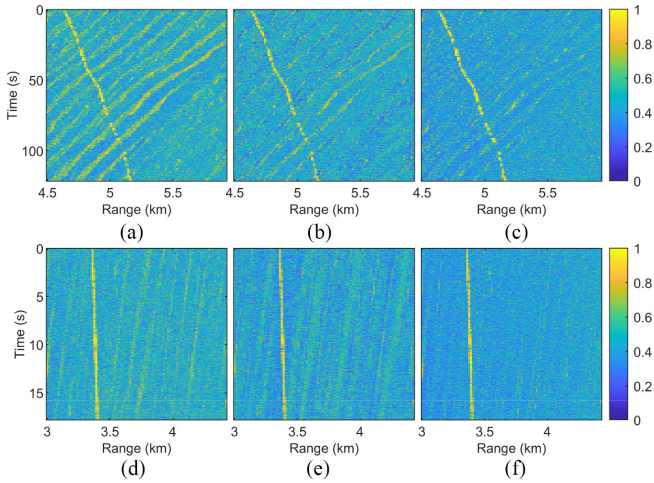
Fig. 10. Values of the test statistics of the three detectors on the range-time scenes of the two datasets. (a) and (d) Adaptive GLRT-LTD under the CGM. (b) and (e) HSS-GLRT-LTD under the BP-CGMM. (c) and (f) FSS-GLRT-LTD under the BP-CGMM.

adaptive GLRT-LTD in (21). Besides the bright traces of the test targets, there are quite a few bright stripes relevant to the crests of long waves on the sea surface, and thus, the detection result contains quite a few false alarms in the bright region of the scenes. The model mismatch of the CGM brings at least three troubles. The false alarm rate fails to be effectively controlled by the theoretical threshold of the GLRT-LTD or decision threshold determined by the Monte-Carlo tests of simulated data. Higher false alarms occur in the bright region of scenes, and large missing probability appears in the dim region of scenes. Since the speckle vectors at the CUT and RCs might have different covariance matrices, the whitening process fails to completely whiten the sea clutter, which degrades its detection ability.

Fig. 10(b) and (e) illustrates the values of the test statistics of the HSS-GLRT-LTD on the whole scene. Since the BP-CGMM characterizes the bi-phase properties of heterogeneous sea clutter well, most of the bright stripes from the crests of long waves in Fig. 10(a) and (d) vanishes. However, there remain a few bright stripes or blurred stripes due to the ignorance of the bi-phase property of Doppler spectra of sea clutter in the whitening process of CUT. Fig. 10(c) and (f) demonstrates the value of the test statistics of the FSS-GLRT-LTD on the whole scene. Except for the bright traces of the test targets, the entire backgrounds are almost homogeneous owing to the matching BP-CGMM and full exploitation of the bi-phase property of both amplitude distribution and Doppler spectrum of sea clutter.

Due to the mismatch of the CGM to heterogeneous sea clutter, both the theoretical threshold in [12] and the threshold from the indirect Monte-Carlo test by simulated clutter data in terms of the parameters of the clutter model [13] fail to control the false alarm rate on the whole scene accurately. For a fair comparison, for the GLRT-LTD, the decision threshold using the test statistic in (21) is tuned to control the false alarm rate on the whole scene at 10^{-3}. For the HSS-GLRT-LTD and FSS-GLRT-LTD, the thresholds in the bright region and dim region are separately

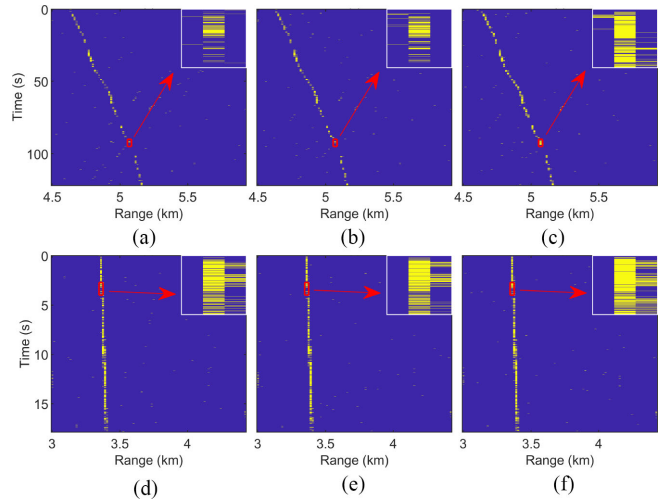| Detector	TFC15-025	TFA17-001
GLRT-LTD	0.2966	0.5826
HSS-GLRT-LTD	0.3327	0.6259
FSS-GLRT-LTD	0.4301	0.6707

Fig. 11. Detected traces of the two test targets from the two datasets by the three detectors at the false alarm rate 10^{-3}: (a) GLRT-LTD on the first dataset. (b) HSS-GLRT-LTD on the first dataset. (c) FSS-GLRT-LTD on the first dataset. (d) GLRT-LTD on the second dataset. (e) HSS-GLRT-LTD on the second dataset. (f) FSS-GLRT-LTD on the second dataset.

tuned to control the false alarm rate in the bright region and dim region at 10^{-3}. The detection probabilities of the three detectors in the two datasets are listed in Table VI. For the first dataset, the HSS-GLRT-LTD using the bi-phase property in amplitude distribution behaves better than the GLRT-LTD, and the FSS-GLRT-LTD using the bi-phase properties in both amplitude distribution and Doppler spectrum is better than the HSS-GLRT-LTD. Fig. 11(a)–(c) plots the detected traces of the test target and local zoomed results at the top right corner of each subfigure. From the local zoomed results, the differences between the three detectors are easily observed. It is also found that the detected traces have some common breaks lasting for several seconds, which probably results from the shadowing effect of swells to the test target in high sea states.

For the second dataset in sea state 4, the results in the second dataset are similar to those in the first dataset for the three detectors. Fig. 11(d)–(f) plots the detected traces of the test target and local zoomed results at the top right corner of each subfigure. The larger detection probabilities in the second dataset show that high sea state is a major reason for degradation of the detection ability of sea-surface small targets at low grazing angles due to the shadowing effect of swells to targets and stronger non-Gaussianity of sea clutter.

V. Conclusion

In this article, a novel BP-CGMM is proposed to model long-wave modulated sea clutter that exhibits strong bi-phase behavior in both amplitude distribution and Doppler spectrum. In the BP-CGMM, the resolution cells in a patch of sea surface are classified into bright region and dim region, and sea clutter in each region is modeled by a CGM with inverse Gamma-distributed texture. Based on the datasets in the CSIR database, the bi-phase behavior of high-resolution sea clutter in amplitude distribution and Doppler spectrum is presented and analyzed in statistics and physics. The BP-CGMM and the corresponding FSS-GLRT-LTD exhibit obvious advantages in goodness-of-fit of sea clutter and detection performance in high sea states in comparison with the CGM of sea clutter and GLRT-LTD. The BP-CGMM and FSS-GLRT-LTD are supplements of the CGM and GLRT-LTD in moderate and high sea states rather than their replacement in all sea states. In low sea states, the CGM with inverse Gamma-distributed texture and GLRT-LTD keep valid owing to their simplification and no systemic delay in processing.

References

[1] S. Brusch, S. Lehner, T. Fritz, M. Soccorsi, A. Soloviev, and B. van Schie, "Ship surveillance with TerraSAR-X," *IEEE Trans. Geosci. Remote Sens.*, vol. 49, no. 3, pp. 1092–1103, Mar. 2011.

[2] M. J.Collins, M. Denbina, B. Minchew, C. E. Jones, and B. Holt, "On the use of simulated airborne compact polarimetric SAR for characterizing oil-water mixing of the deepwater horizon oil spill," *IEEE J. Sel. Topics Appl. Earth Observ. Remote Sens.*, vol. 8, no. 3, pp. 1062–1077, Mar. 2015.

[3] J. Carretero Moya, J. Gismero Menoyo, A. Asensio-Lopez, and A. Blanco-Del-Campo, "Small-target detection in high-resolution heterogeneous sea-clutter: An empirical analysis," *IEEE Trans. Aerosp. Electron. Syst.*, vol. 47, no. 3, pp. 1880–1898, Jul. 2011.

[4] S. Xu, J. Zhu, J. Jiang, and P. Shui, "Sea-surface floating small target detection by multifeature detector based on isolation forest," *IEEE J. Sel. Topics Appl. Earth Observ. Remote Sens.*, vol. 14, pp. 704–715, 2021.

[5] D. Tao, A. Doulgeris, and C. Brekke, "A segmentation-based CFAR detection algorithm using truncated statistics," *IEEE Trans. Geosci. Remote Sens.*, vol. 54, no. 5, pp. 2887–2898, May 2016.

[6] W. Wang, D. Xiang, Y. Ban, J. Zhang, and J. Wan, "Superpixel segmentation of polarimetric SAR images based on integrated distance measure and entropy rate method," *IEEE J. Sel. Topics Appl. Earth Observ. Remote Sens.*, vol. 10, no. 9, pp. 4045–4058, Sept. 2017.

[7] D. Xiang, Y. Ban, W. Wang, and Y. Su, "Adaptive superpixel generation for polarimetric SAR images with local iterative clustering and SIRV model," *IEEE Trans. Geosci. Remote Sens.*, vol. 55, no. 6, pp. 3115–3131, Jun. 2017.

[8] M. Martorella, D. Pastina, F. Berizzi, and P. Lombardo, "Spaceborne radar imaging of maritime moving targets with the Cosmo-SkyMed SAR system," *IEEE J. Sel. Topics Appl. Earth Observ. Remote Sens.*, vol. 7, no. 7, pp. 2797–2810, Jul. 2014.

[9] D. Yang, D. Du, H. Liu, Y. Wang, and M. Gu, "Extended geometrical perturbation based detectors for PolSAR image target detection in heterogeneously patched regions," *IEEE J. Sel. Topics Appl. Earth Observ. Remote Sens.*, vol. 12, no. 1, pp. 285–301, Jan. 2019.

[10] T. Li, Z. Liu, R. Xie, L. Ran, and J. Wang, "Ship detection for polarimetric SAR images based on p0 mixture model," *IEEE J. Sel. Topics Appl. Earth Observ. Remote Sens.*, vol. 12, no. 6, pp. 1812–1824, Jun. 2019.

[11] E. Jay, J. P. Ovarlez, D. Declercq, and P. Duvaut, "BORD: Bayesian optimum radar detector," *Signal Process*, vol. 83, no. 6, pp. 1151–1162, 2003.

[12] K. Sangston, F. Gini, and M. Greco, "Coherent radar target detection in heavy-tailed compound-Gaussian clutter," *IEEE Trans. Aerosp. Electron. Syst.*, vol. 48, no. 1, pp. 64–77, Jan. 2012.

[13] P. L. Shui, M. Liu, and S. W. Xu, "Shape-parameter-dependent coherent radar target detection in K-distributed clutter," *IEEE Trans. Aerosp. Electron. Syst.*, vol. 2, no. 1, pp. 451–465, Feb. 2016.

[14] S. N. Shi, X. Liang, P. L. Shui, J. K. Zhang, and S. Zhang, "Low-velocity small target detection with Doppler-guided retrospective filter in high-resolution radar at fast scan mode," *IEEE Trans. Geosci. Remote Sens.*, vol. 57, no. 11, pp. 8937–8953, Nov. 2019.

[15] M. Greco, P. Stinco, F. Gini, and M. Rangaswamy, "Impact of sea clutter nonstationarity on disturbance covariance matrix estimation and CFAR detector performance," *IEEE Trans. Aerosp. Electron. Syst.*, vol. 46, no. 3, pp. 1502–1513, Jul. 2010.

[16] K. D. Ward, R. J. A. Tough, and S. Watts, *Sea Clutter: Scattering, the K-Distribution and Radar Performance*. Stevenage, U.K.: Inst. Eng. Technol., 2013, pp. 1–40.

[17] M. Greco, F. Bordoni, and F. Gini, "X-band sea-clutter nonstationarity: Influence of long waves." *IEEE J. Ocean. Eng.*, vol. 29, no. 2, pp. 269–283, Apr. 2004.

[18] S. Watts, K. D. Ward, and R. J. A. Tough, "The physics and modelling of discrete spikes in radar sea clutter," in *Proc. IEEE Int. Radar Conf.*, 2005, pp. 72–77.

[19] D. Yunhan, "Distribution of X-band high resolution and high grazing angle sea clutter," Australian Government Dept. Defence, Fairbairn, Australia, DSTO-RR-0316, 2006.

[20] L. Rosenberg and S. Bocquet, "Comparison of bi-modal coherent sea clutter simulation techniques," *IET Radar, Sonar Navigation*, vol. 13, no. 9, pp. 1519–1529, 2019.

[21] R. Romeiser, W. Alpers, and V. Wismann, "An improved composite surface model for the radar backscattering cross section of the ocean surface: 1. Theory of the model and optimization/validation by scatterometer data," *J. Geophys. Res. Oceans*, vol. 102, no. C11, pp. 25237–25250, 1997.

[22] C. Chae and J. T. Johnson, "A study of sea surface range-resolved doppler spectra using numerically simulated low-grazing-angle backscatter data," *IEEE Trans. Geosci. Remote Sens.*, vol. 51, no. 6, pp. 3452–3460, Jun. 2013.

[23] Y. Y. Yurovsky, V. N. Kudryavtsev, B. Chapron, and S. A. Grodsky, "Modulation of Ka-band doppler radar signals backscattered from the sea surface," *IEEE Trans. Geosci. Remote Sens.*, vol. 56, no. 5, pp. 2931–2948, May 2018.

[24] Y. Wei, L. Guo, and J. Li, "Numerical simulation and analysis of the spiky sea clutter from the sea surface with breaking waves," *IEEE Trans. Antennas Propag.*, vol. 63, no. 11, pp. 4983–4994, Nov. 2015.

[25] J. Wang and X. Xu, "Simulation of correlated low-grazing-angle sea clutter based on phase retrieval," *IEEE Trans. Geosci. Remote Sens.*, vol. 53, no. 7, pp. 3917–3930, Jul. 2015.

[26] D. Orlando and G. Ricci, "Adaptive radar detection and localization of a point-like target," *IEEE Trans. Signal Process.*, vol. 59, no. 9, pp. 4086–4096, Sep. 2011.

[27] S. P. Lu, W. Yi, W. J. Liu, G. L. Cui, L. J. Kong, and X. B. Yang, "Data-dependent clustering-CFAR detector in heterogeneous environment," *IEEE Trans. Aerosp. Electron. Syst.*, vol. 54, no. 1, pp. 476–485, Feb. 2018.

[28] F. Bandiera, O. Besson, and G. Ricci, "Knowledge-aided covariance matrix estimation and adaptive detection in compound-Gaussian noise," *IEEE Trans. Signal Process.*, vol. 58, no. 10, pp. 5391–5396, Oct. 2010.

[29] S. Bidon, O. Besson, and J. Y. Tourneret, "A Bayesian approach to adaptive detection in nonhomogeneous environments," *IEEE Trans. Signal Process.*, vol. 56, no. 1, pp. 205–217, Jan. 2008.

[30] S. D. Han, A. D. Maio, V. Carotenuto, L. Pallotta, and X. T. Huang, "Censoring outliers in radar data: An approximate ML approach and its analysis," *IEEE Trans. Aerosp. Electron. Syst.*, vol. 55, no. 2, pp. 534–546, Apr. 2019.

[31] Accessed: Dec. 13, 2018. [Online]. Available: http://www.csir.co.ca/small_target_detection

[32] A. Aprile, E. Grossi, M. Lops, and L. Venturino, "Track-before-detect for sea clutter rejection: Tests with real data," *IEEE J. Sel. Topics Appl. Earth Observ. Remote Sens.*, vol. 53, no. 3, pp. 1035–1045, Jun. 2016.

[33] Accessed: Oct. 11, 2012. [Online]. Available: http://soma.crl.mcmaster.ca/ipix

[34] J. Carretero-Moya, J. Gismero-Menoyo, Á. Blanco-del-Campo, and A. Asensio-Lopez, "Statistical analysis of a high-resolution sea-clutter database," *IEEE Trans. Geosci. Remote Sens.*, vol. 48, no. 4, pp. 2024–2037, Apr. 2010.

[35] P. L. Herselman, "An analysis of X-band calibrated sea clutter and small boat reflectivity at medium-to-low grazing angles," *Int. J. Navigation Observation*, vol. 2008, 2008, Art. no. 347518.

[36] M. E. M. Abdelaziz, T. Chonavel, A. Aissa El Bey, A. Belouchrani, and M. Hamadouche, "Sea clutter texture estimation: Exploiting decorrelation and cyclostationarity," *IEEE Trans. Aerosp. Electron. Syst.*, vol. 49, no. 2, pp. 726–743, Apr. 2013.

[37] K. Ing, M. R. Morelande, S. Suvorova, and B. Moran, "Parametric texture estimation and prediction using measured sea clutter data," *IET Radar, Sonar Navigation*, vol. 10, no. 3, pp. 449–458, 2016.

[38] M. C. Haller and D. R. Lyzenga, "Comparison of radar and video observations of shallow water breaking waves," *IEEE Trans. Geosci. Remote Sens.*, vol. 41, no. 4, pp. 832–844, Apr. 2003.

[39] T. Lamont Smith, T. Waseda, and C. Rheem, "Measurements of the Doppler spectra of breaking waves," *IET Radar, Sonar Navigation,* vol. 1, no. 2, pp. 149–157, 2007.

[40] R. Gangeskar, "An algorithm for estimation of wave height from shadowing in X-band radar sea surface images," *IEEE Trans. Geosci. Remote Sens.*, vol. 52, no. 6, pp. 3373–3381, Jun. 2014.

[41] S. Bocquet, L. Rosenberg, and C. H. Gierull, "Parameter estimation for a compound radar clutter model with trimodal discrete texture," *IEEE Trans. Geosci. Remote Sens.*, vol. 58, no. 10, pp. 7062–7073, Oct. 2020.

[42] H. Yu, P. Shui, and K. Lu, "Outlier-robust tri-percentile parameter estimation of K-distributions," *Signal Process*, vol. 181, 2021, Art. no. 107906.

[43] T. Kailath, "The divergence and Bhattacharyya distance measures in signal selection," *IEEE Trans. Commun. Tech.*, vol. 15, no. 1, pp. 52–60, Feb. 1967.

[44] M. A. Stephens, "EDF statistics for goodness of fit and some comparisons," *J. Amer. Statistical Assoc.*, vol. 69, no. 347, pp. 730–737, 1974.

[45] F. Gini and M. Greco, "Covariance matrix estimation for CFAR detection in correlated heavy tailed clutter," *Signal Process,* vol. 82, no. 12, pp. 1847–1859, 2002.

Peng-Lang Shui received an M.S. degree in mathematics from Nanjing University, China, in 1992 and a Ph.D. degree in electrical engineering from Xidian University, Xi'an, China, in 1999.

He is now a Professor at the National Laboratory of Radar Signal Processing, Xidian University. His research interests include sea clutter modeling and analysis, radar target detection, and image processing.
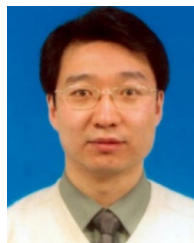
Hong-Tao Su received the B.S., M.S., and Ph.D. degrees in electronics engineering from Xidian University, Xi'an, China, in 1997, 2000, and 2005, respectively.

He is currently a Professor with the National Laboratory of Radar Signal Processing, Xidian University. His main research interests include high-frequency over-the-horizon radar signal processing, adaptive array signal processing, and statistical signal processing.

Xiang Liang was born in Hebei, China, in 1994. He received the B.S. degree in electrical engineering from Xidian University, Xi'an, China, in 2017, where he is currently working toward the Ph.D. degree with the National Laboratory of Radar Signal Processing.

His research interests include radar signal simulation and weak target detection in sea clutter.